Nanoscale

Phase Transformation among TiO2 Polymorphs

Journal:	*Nanoscale*
Manuscript ID	NR-ART-08-2020-006226.R1
Article Type:	Paper
Date Submitted by the Author:	09-Oct-2020
Complete List of Authors:	Song, Miao; Pacific Northwest National Laboratory Lu, Zexi; Pacific Northwest National Laboratory Li, Dongsheng; Pacific Northwest National Laboratory

Nanoscale

COMMUNICATION

Phase Transformations among TiO_2 Polymorphs

Miao Song, ‡, [a] Zexi Lu, ‡, [a] Dongsheng Li*[a]

Received 00th January 20xx,
Accepted 00th January 20xx

DOI: 10.1039/x0xx00000x

www.rsc.org/

Polymorphs widely exist in nature and synthetic systems and are well known to determine material properties. Understanding phase transformation mechanisms among polymorphs enables the design of structures and tuning of phases to tailor material properties. However, current understanding is limited due to the lack of direct observations of the structural evolution at the atomic scale. Here, integrating (semi) in situ transmission electron microscopy and density functional theory, we report atomic structural evolutions of phase transformation from anatase (A) to rutile (R), brookite (B), R-phase, and TiO. Besides the consistent paths with previous reports, we discover several unreported paths, including a [001] direction and (020) plane of anatase to $[100]_R$ and $(0\bar{1}1)_R$ of rutile, respectively, ($[001]_A||[100]_R$, $(020)_A||(0\bar{1}1)_R$) and $[001]_A||[001]_B$, $(020)_A||(220)_B$. Density functional theory analysis elucidates atomic structural evolution during the processes and over 16% of Ti-O bonds break and reform during the processes with energy barriers of ~0.7-1.0 eV per TiO_2 formula unit. Under electron-beam irradiation, anatase particles transform into TiO_2-R phase or TiO at high or room temperature, respectively. We also reveal the anisotropic nature of the electron-beam effect, which is seldom discussed: dependence of crystallographic orientation with respect to electron-beam irradiation direction. Understanding the atomic structural evolution sheds light on interpreting and controlling TiO_2 polymorphs and interface structures for various applications. The revealed electron-beam effects in our work provide guidance for in situ transmission electron microscopy studies.

Polymorphs widely exist in nature and synthetic systems of crystalline materials, such as polymers [1], minerals [2], and metals [3]. Crystal phases determine materials' properties and functional applications, such as photocatalysis [4], clinical drugs [5], energy storage [6], mechanical deformation [7], etc. For example, anatase is known to have better photoactivity than rutile because charge carriers excite deeper in the bulk contribute to surface reactions in anatase than that in rutile [8]. Hematite (α-Fe_2O_3) and maghemite (γ-Fe_2O_3) present a significant difference in magnetic properties [9]. More recently, the phase-function relationship has attracted attention for improving material properties. Black TiO_2 has been reported with greatly increased solar absorption by introducing an amorphous structure in the surface layers of nanophase TiO_2 [10]. The interfaces between anatase and brookite can greatly enhance the photocatalytic activity for photocatalytic H_2 production [11]. Photocatalytic efficiency was optimized by mixed phases of anatase and rutile, such as Degussa P-25 (~85 wt% anatase (A) and ~15 wt% rutile (R)) [4, 12]. In addition, phase transformation plays a key role in the material synthesis and particle assembly process, such as oriented attachment [13]. For example, rutile nanowires and (101) twin interfaces form through the oriented attachment of $(103)_A$ facets of anatase particles onto $(101)_R$ facets of rutile particles and the following phase transformation from anatase to rutile [13].

Understanding phase transformation mechanisms enables us to control materials synthesis and processing and thus to design materials phases with tailored properties. Here, we investigate the phase transformation mechanism among TiO_2 polymorphs due to its extensive applications, such as photocatalysis [14-16], solar energy conversion [17-18], energy storage [19-20], biomedicine [21-22], and nonvolatile memory [23-24]. Phase transformation of TiO_2 has been widely investigated focusing on factors such as temperature [25], particle size [26-28], evolution sequence [29], and surface chemistry [30], etc. For example, it has been reported that aggregated anatase particles can transform into rutile irreversibly at elevated temperatures (400–1200°C) [25]. For a single anatase particle, the anatase phase is stable up to 1000°C [31]. A generally recognized anatase to rutile transformation (ART) mechanism was proposed by Penn et al. [32] and Zhang et al. [33] that rutile phase nucleates at anatase $\{112\}$ twin boundary due to the low activation barrier. The

[a] Physical and Computational Sciences Directorate, Pacific Northwest National Laboratory, Richland, WA 99352, USA. E-mail: Dongsheng.Li2@pnnl.gov
‡These authors contributed equally.
†Electronic Supplementary Information (ESI) available: [Rutile identification; Density functional theory (DFT) calculations; Another ART process identified by in situ SAED TEM experiment; ABT phase transformation; E-beam induced phase transformation from anatase to R-phase and R-phase back to anatase at high temperature; E-beam induced reduction of TiO2 to TiO; The need of in situ TEM investigation; Morphologies of various anatase nanoparticles; Experimental procedures; Crystal structures of various phases.]. See DOI: 10.1039/x0xx00000x

process of rutile nucleation and growth involves displacement of one half Ti atoms and rupture of 7 of 24 Ti-O bonds in an unit cell [32], keeping the orientation relationship of $\langle 010\rangle_A||\langle 110\rangle_R$, $\{112\}_A||\{010\}_R$. Other ART orientation relationships also were reported in previous studies, such as $\langle 110\rangle_A||\langle 011\rangle_R$, $\{112\}_A||\{200\}_R$[34] (Table S1).

All these studies mainly are focused on aggregated particles by postmortem experiments, which do not yield information about intermediate phases, particle aggregation and rotation, morphological evolution, and interface migration at high temperatures. Therefore, to some extent, previously reported mechanisms are hypothetical. More importantly, because information about the phase transformation process of a single particle is lacking, little is known regarding key information needed for tuning materials structures, such as the evolution of atomic structures, twin interface formation, and intermediate phases during phase transformation processes. Twin interface formation not only plays an important role during TiO_2 phase transformation [32] but also is employed to tune particle morphology [35-36]. The twinning process of rutile can be realized by topotaxial growth [37-38], deformation [38-39], and orientation attachment [13, 40-41]. However, the twinning mechanism during the ART process is still unclear. Here, we employed a recently developed double tilt TEM holder equipped with the capability of heating up to 1100°C to track the phase transformation of a single particle and investigate the phase transformation relationship of various TiO_2 polymorphs of anatase, rutile, brookite (B), R-phase, and TiO. Twinning mechanisms during the ART process also were discussed.

Generally, the thermodynamical stability of rutile is higher than that of anatase and brookite when the particle size is larger than tens of nanometers [42]. After heating at 900–950°C for 280 min, the square platelet-shaped anatase particle (~ 200 nm, Fig. 1a-b) evolves into a particle with a hexagonal shape (Fig. 1c-d), which is identified as rutile by fast Fourier transform (FFT) diffraction patterns (DPs) from two different zone axes obtained by tilting the sample (Fig. 1d and S1). By tracking the

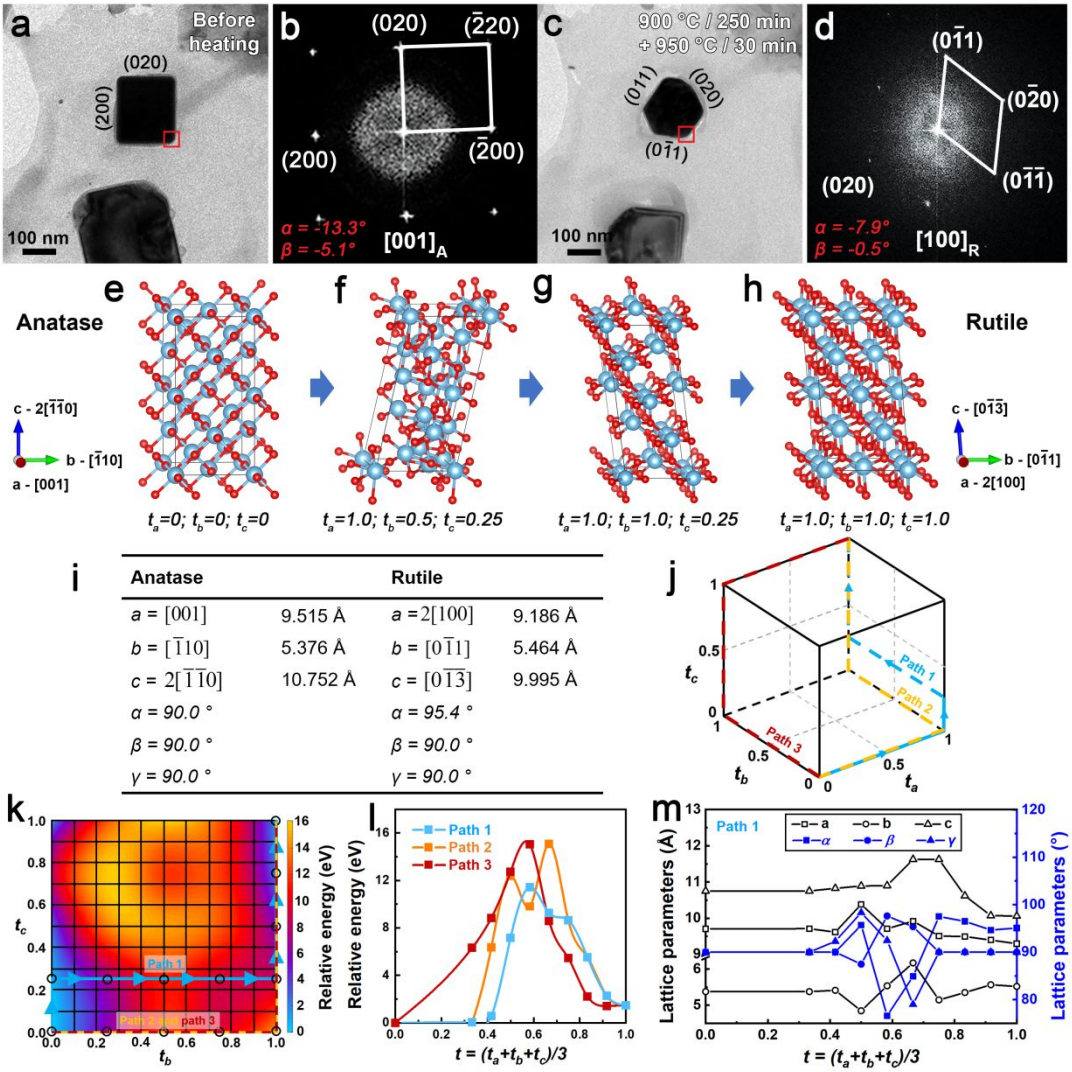

Fig. 1 ART following the pathway of $[001]_A||[100]_R$,$(020)_A||(0\bar{1}1)_R$. (a) and (c) Bright field (BF) images of a (001)-platelet before and after heating at 950° for 30 min, respectively. (b) and (d) FFT images of HRTEM images of the red-boxed areas in (a) and (c), respectively. (e–h) 3D crystal structures of anatase, hypothetical intermediate phases, and rutile showing atomic rearrangement during the ART process from $[001]_A$ to$[100]_R$. (i) Lattice parameters of anatase and rutile employed for density functional theory (DFT) simulation. (j) Three-dimensional (3-D) map showing three paths employed for DFT simulation. (k) Two-dimensional map of lowest potential energy surface according to t_b and t_c. The simulated ART path 1, 2, and 3 were highlighted by the cyan, orange, red lines, respectively. (l) Energy evolution during ART simulated by DFT. (m) Evolution of lattice parameters of the path 1 during the DFT simulated ART process.

same locations of the particle before and after the heating process, FFT DPs from high-resolution transmission electron microscopy (HRTEM) images confirm that $[001]_A$ of anatase transforms into $[100]_R$ of rutile, $[001]_A$ || $[100]_R$, and $(020)_A$ plane transforms into $(0\bar{1}1)_R$, $(020)_A$ || $(0\bar{1}1)_R$ (Fig. 1b, d, and Fig. S1), consistent with the shape evolution as indicated by the trace of the original anatase square shape around the hexagonal projection (Fig. 1c). This path differs from previously reported ART orientation relationships [32, 34] (Table S1).

To explore the details of atomic movements, bond breaking and reformation, and energy barriers, we perform DFT calculations (see experimental and SI-section 2 for details). Based on the above ART orientation relationship, we first build the corresponding supercells of anatase and rutile; that is, $[001]$, $[\bar{1}10]$, and $2[\bar{1}\bar{1}0]$ of anatase correspond to $2[100]$, $[0\bar{1}1]$, and $[0\bar{1}\bar{3}]$ of rutile as the cell parameters of a, b, and c, respectively (Fig. 1i). Based on the corresponding supercells, we calculate possible intermediate structures along with the three directions from t_a=t_b=t_c=*0* (anatase) to t_a=t_b=t_c=*1* (rutile), where t_a, t_b, *and* t_c, are the transition steps along *a*, *b*, and *c* directions, respectively (Fig. 1e-h, See SI-section 2 for details). Five steps are introduced along *b* and *c* directions, with Δt_b=Δt_c=0.25. Only two steps (Δt_a=1) are introduced along *a* direction since the displacements of Ti atoms along this direction are negligible. Therefore, altogether there are 50 possible intermediate structures. We select the lowest-energy barrier pathway as the most feasible pathway (path 1, Fig. 1j, and k). The DFT calculation shows that the anatase supercell (Fig. 1e) shears to the right first with the formation of a possible intermediate phase (Fig. 1f), then shears to the left (Fig. 1g), and finally transits into rutile (Fig. 1h), also shown by the lattice parameter changes of α, β, and γ (Fig. 1m). In addition, there are obvious lattice expansions or compressions during the transformation. For example, expansions of *a* (7.0%), *b* (14.8%), and *c* (8.1%) provide extra space for rearrangement of oxygen atoms at *t*=0.5 (t_a=*1*, t_b=*0.25*, t_c=*0.25*), *t*=0.66 (t_a=*1*, t_b=*0.75*, t_c=*0.25*), and *t*=0.66-0.75 (t_a=*1*, t_b=*0.75-1*, t_c=*0.25*), respectively (Fig. 1m). These strains are accompanied by Ti-O bond breaking and reformation, such as 2.0%, 24.0%, and 16.7% Ti-O bonds breaking at *t*=0.58 (t_a=*1*, t_b=*0.5*, t_c=*0.25*), 0.66 and 0.75, respectively (assuming Ti-O bonds with a length larger than 2.5 Å are broken). All these bonds recombine at *t*=0.83 (t_a=*1*, t_b=*1*, t_c=*0.5*) and converge to rutile bond lengths afterwards. During this lattice deformation and bond-breaking-recombination process, the energy barrier is ~0.71 eV per TiO_2 formula unit (path 1, Fig. 1l). For comparison, we exam two extreme pathways: (1) path *a-b-c* (path 2) where Ti atomic displacements happen along *a* direction only first, then *b* direction only, and finally *c* direction, and (2) path *b-c-a* (path 3) where the displacements of Ti atoms along *b* first, then *c*, and finally *a* direction (Fig. 1j). The corresponding energy barriers are 0.77 and 0.94 eV per TiO_2 formula unit for path 2 and path 3, respectively (Fig. 1l). The higher energy barriers probably originate from the slightly large change (Fig. S2a-c) in cell shapes (lattice parameters) of the transitional structures compared with the optimal path 1 (Fig. 1m), which has much smoother transitions.

Besides the above ART process, by in situ selected area electron diffraction (SAED) TEM (SI-section 3), we also observe a different ART pathway of $[001]_A||[11\bar{2}]_R$, $(020)_A||(1\bar{1}0)_R$. The in situ SAED patterns show multiple sets of patterns, instead of one single crystal pattern (Fig. S3), indicating that the single crystal transforms into a polycrystal and some unknown intermediate phases during ART process; that is, the new phases nucleate and grow simultaneously at various locations in the bulk, instead of directly transforming from one phase to another trigged by one nucleus. This pathway is equivalent to previously reported $\langle 110\rangle_A||\langle 011\rangle_R$,$\{112\}_A||\{200\}_R$[34] by postmortem experiments (Fig. S3e). Based on various paths of the ART process reported previously [32, 34] (Table S1) and observed in our experiments (Fig.1 and Fig. S3), we hypothesize that the path is related to the particle size, morphology, heating conditions (heating rate and temperature).

In our semi-in situ experiment, approximately 9% rutile particles (total ~100 particles) were found with lowest-energy $\{101\}_R$ twin structures [43] based on a statistical analysis of twin contrast in BF images or HRTEM images. We propose three mechanisms for twin interface formation during ART process.

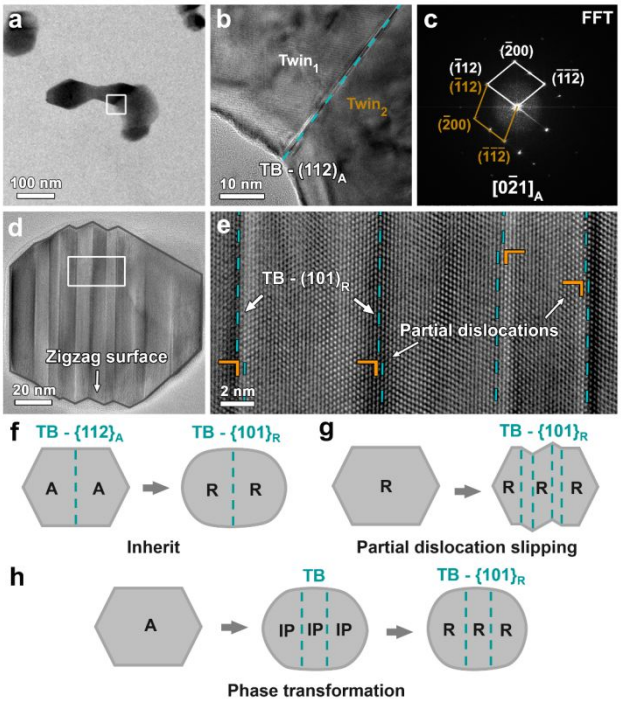

Fig. 2 Twinning mechanisms of a $\{101\}_R$ twin during the ART process. (a) BF image of an octahedral nanoparticle with a twin interface. (b) HRTEM image of the white-boxed area in (a), showing the $\{112\}_A$twin interface (cyan-dashed lines). (c) FFT image of (b) verifying the twin relationship. (d) BF image of a twinned rutile nanoparticle formed after heating at 1100°C for 50 min. The zigzag edges are denoted by gray lines. (e) HRTEM images of the white boxed area in (d) showing some partial dislocations (denoted by yellow "⊥") on twin boundaries. (f–h) Schematic illustration to show three possible twinning mechanisms of $\{101\}_R$ twin. IP denotes intermediate phase.

For the first mechanism (i.e., inheritance from the original anatase), $\{112\}_A$ twin interfaces are common in anatase particles (Fig. 2a-c) [32-33]. During the pathway of $\langle 001\rangle_A||\langle 100\rangle_R$, $\{020\}_A||\{0\bar{1}1\}_R$ (Fig. 1), the $\{112\}_A$ plane evolves into a $\{101\}_R$ plane (Fig. S4), leading to existing $\{112\}_A$ twin interfaces in anatase particles [44] (Fig. 2a-c) transform into rutile $\{101\}_R$ twin interfaces (Fig. 2f). For the second mechanism, a twin structure is induced by partial dislocation slipping, which is known as a general pathway to form twin interfaces [45]. In our experiments, we observe zigzag surface near twin boundaries (Fig. 2d-e) in rutile crystals, which is a typical morphology resulting from partial dislocations slipping of planes [46], indicating twin

formation via a $\frac{5}{12}\{101\}\langle 101\rangle$ partial dislocation ($\{101\}$ slipping plane moving on $\langle 101\rangle$ direction with a magnitude of $\frac{5}{12}\langle 101\rangle$) [39] in rutile crystals. For the third mechanism, we propose that atoms move in opposite directions along a specific anatase plane, which will be the twin boundary of a rutile particle after ART (Fig. 2h). During different ART pathways, various anatase planes can transform into a rutile $\{101\}$ plane. The twin formation depends on the energy barrier and the feasibility of opposite moving of Ti atoms.

Besides ART, we also study the ABT phase transformation at a lower temperature of 900°C via a semi-in-situ heating experiment. After heating at 900°C for 240 min (Fig. 3a-b), the brookite phase (Fig. 3c) forms within the anatase platelet particle (~170 nm, Fig. 3a-b). Brookite was identified by FFT DP (Fig. 3b inset) of the HRTEM image and further confirmed by FFT DPs obtained by tilting samples to three different zone axes (Fig. S5a-c). The FFT DPs (Fig. 3a and Fig. S5a-c) and HRTEM image (Fig. 3c) show that this ABT follows $[001]_A||[001]_B$,$(020)_A||(220)_B$, leading to excellent coherent interfaces of $(2\bar{2}0)_B/(200)_A$ (Fig. 3d) and $(220)_B/(020)_A$ due to the perfect match of theoretical lattice spacings (d) of anatase ($d_{(200)A} = d_{(020)A} = 1.892$Å, $d_{(002)A} = 4.758$Å) to brookite ($d_{(220)B} = d_{(2\bar{2}0)B} = 1.872$Å, $d_{(020)B} = 4.580$Å), respectively, with 1.0%–3.7% lattice mismatch and volume variation of -5.9%. This small lattice deformation in 3-D space facilitates the formation of the brookite in anatase platelet particles. Based on 18 examples, the morphology barely changes during ART processes (Fig. 3a-b, Fig. S5), unlike the obvious morphology change during ART processes (Fig. 1). This path differs from previously reported ABT orientation relationships [46, 47] (Table S1).

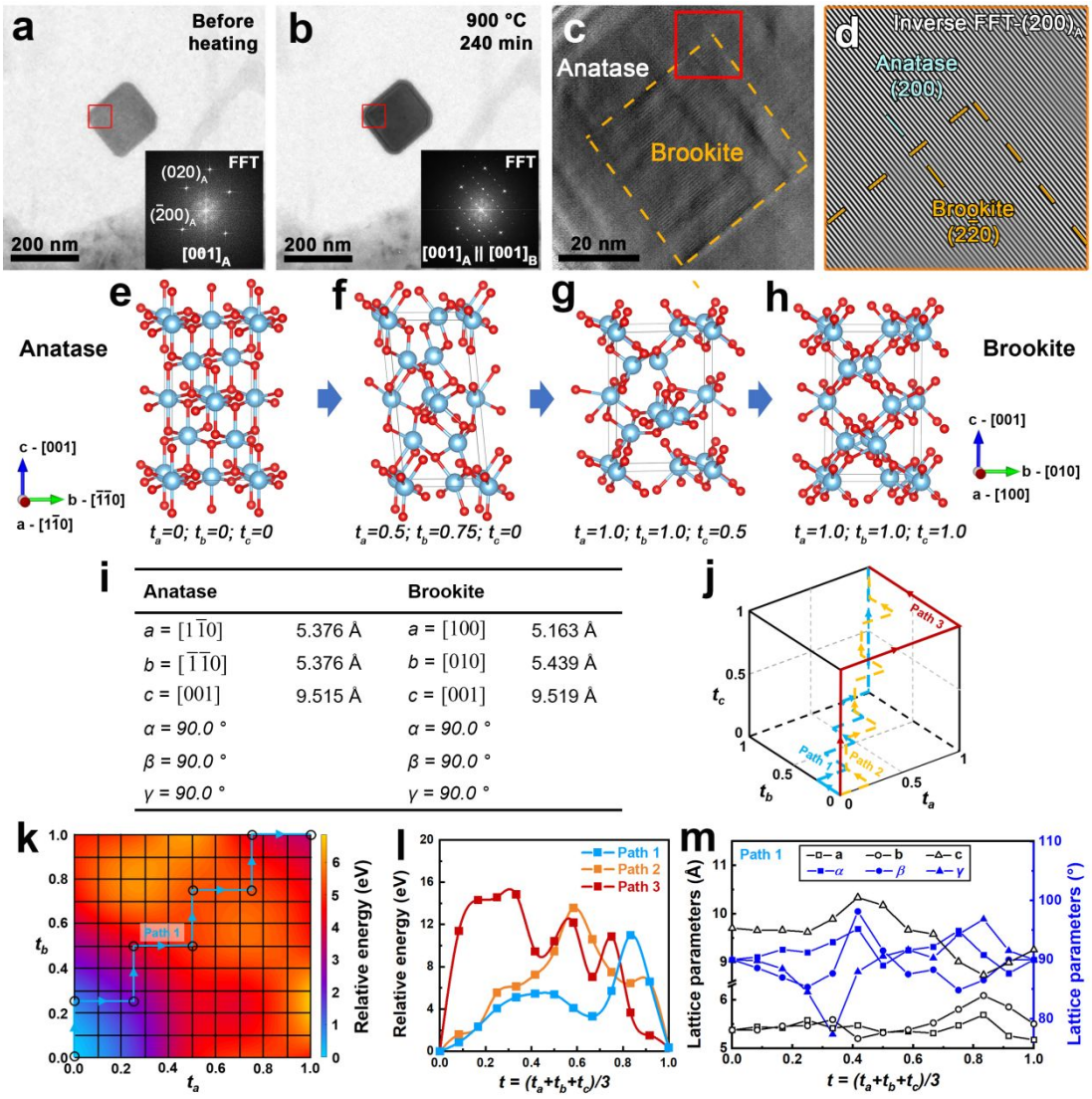

Fig. 3 ABT following the pathway of $[001]_A||[001]_B$,$(020)_A||(220)_B$. (a) and (b) BF images of a (001)-platelet before and after heating at 900°C for 240 min, respectively, showing no obvious morphology change. Insets are FFT images of corresponded red-boxed areas. (c) HRTEM images of the red-boxed area in (b) showing a rectangular brookite (denoted by yellow-dashed box) embedded in the anatase nanoparticle. (d) Inverse FFT images of $(200)_A$, showing perfect match of anatase and brookite lattices. (e–h) 3-D crystal structures of anatase, hypothetical intermediate phases, and brookite showing atomic rearrangement during the ABT process from $[001]_A$ to $[001]_B$. (i) Lattice parameters of corresponding supercells of anatase and brookite. (j) 3-D map showing the three paths employed for DFT simulation. (k) Two-dimensional map of lowest potential energy surface according to t_a and t_b. The lowest-energy barrier ABT path (path 1) is highlighted by the cyan line. (l and m) Evolution of energy and lattice parameters, respectively, calculated by DFT.

Same as the ART process, we further investigate the ABT process using DFT calculations. Five transitional steps are introduced in all three directions (Δt_a=Δt_b=Δt_c=0.25), resulting in 125 possible intermediate structures, among which the transitional structures with the lowest energy barrier (Path 1, Fig. 3e-k) are chosen as the most likely pathway. During the simulated ABT process (path 1), the anatase supercell (Fig. 3e) shows a shear deformation first (Fig. 3f) as observed during the ART process (Fig. 1f), then shears back (Fig. 3g), and transits into brookite (Fig. 3h). Lattices deform obviously at t=0.4 and 0.83 (Fig. 3m), corresponding to two energy barriers at the same t=0.4 and 0.83 (Fig. 3l). For example, at t=0.41 (t_a=0.5, t_b=0.75, t_c=0), there is a lattice expansion of c (6.5%). At t=0.83 (t_a=1, t_b=1, t_c=0.5), a lattice compression of c (10.0%) and lattice expansions of a (5.9%) and b (13.2%) occur (Fig. 3m). Correspondingly, the volume increases by 7.0%, providing extra space for the rearrangement of oxygen atoms. Nearly the entire ABT process of t >=0.17 is accompanied by Ti-O bond breaking and reformation, with its peak at t=0.83 where 18.3% of the bonds are broken. The energy barrier of ~0.96eV per TiO_2 formula unit also appears here. For comparison, we show two other energy less favorable pathways: diagonal path (path 2, Fig. 3j) and path c-a-b (path 3, Fig. 3j). The corresponding energy barriers are 1.69 and 1.86 eV per TiO_2 formula unit for paths 2 and 3 (Fig. 3l), respectively. The high energy barrier originates from the more dramatic cell shape change (Fig. S2d-f) as compared with the pathway of the lowest energy barrier.

Notably, the experimental phase transformation also involves morphology evolution, similar to that in the ART process, and is supposed to be affected by particle size, exposed surfaces, local environment (e.g., strains induced by lattice mismatch among original, intermediate, and final phases), heating conditions (e.g., heating rate and temperature), etc. These factors are not manifested in the DFT calculation. Furthermore, because of the periodic boundary conditions, the calculated transformation pathways represent homogeneous transitions of all unit cells in the entire bulk material. On the other hand, in experiments, the transformation can happen locally in a few unit cells first and then gradually propagate throughout the particles. Consequently, all unit cells do not overcome the energy barrier simultaneously, resulting in an easier and smoother transformation. Therefore, it is expected that the calculated energy barrier would be higher than that obtained from experiments. The obtained atomic structural evolution represents the most likely one among the 50 (ART) or 125 (ABT) feasible pathways built based on TEM observation.

To study e-beam effects, we introduce e-beam irradiation at a high temperature. We first heat the sample without the e-beam at 950°C for ~1046 s, during which no obvious morphological and structural changes are observed. However, R-phase immediately nucleates and grows (within 10 s) when the e-beam is introduced (Fig. 4a-c and S5a-c). R-phase is confirmed by multiple DPs obtained by tilting the particle to two different zone axes (Fig. S5d-e). Time-sequenced HRTEM images (Fig. 4a-c) show that R-phase nucleates at the surface of the anatase particle and grows by steps along the interface of $(10\bar{1})_A/(100)_{RP}$ (yellow arrows in Fig. 4b). The height of steps is multiple of $2d_{(100)RP}$ (red arrows in Fig. 4a). The phase

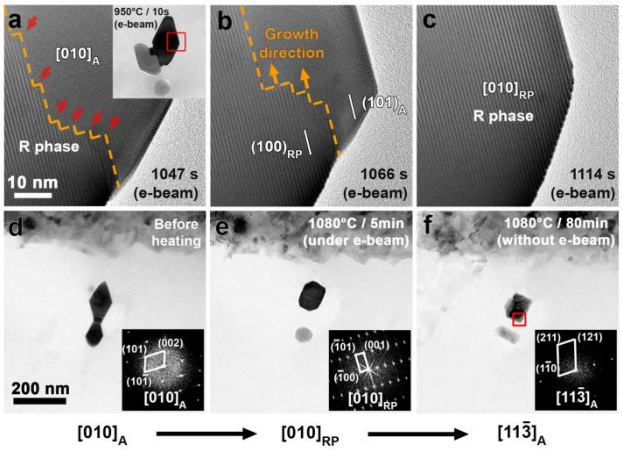

Fig 4. Electron-beam induced phase transformation at high temperature. (a–c) Time-sequenced in situ HRTEM images (red-boxed area in inset of (a)), showing phase transformation formation process from anatase to R-phase. The interface between anatase and R-phase is denoted by yellow-dashed lines. (d–f) BF images and corresponding FFT DPs (insets) showing the original morphology, phase change, and orientation of nanoparticles before and after heating at 1080°C for 5 min under the e-beam, and 1080°C for 80 min without e-beam, respectively.

transformation follows $[010]_A||[010]_{RP}$, $(10\bar{1})_A||(\bar{1}00)_{RP}$ (Fig. 4d-e). The R-phase induced by the e-beam is not stable and transforms back into the anatase phase during further heating and e-beam exposure (Fig. 4d-e). The anatase phase is confirmed by multiple FFT DPs by tilting the sample to three different zone axes (Fig. S6f-g). However, the transformation back to anatase is not a reversible path and follows the transformation relationship of $[010]_{RP}||[11\bar{3}]_A$, $(\bar{1}00)_{RP}||(1\bar{1}0)_A$ (Fig. 4e-f). Overall, under e-beam irradiation and heating, the anatase phase transforms into a different orientation of anatase through R-phase, i.e. $[010]_A||[11\bar{3}]_A$.

An e-beam also can reduce Ti^{4+} into Ti^{2+} at room temperature (Fig. 5 and Fig. S7-8) [48] with small particles of ~20 nm. The TiO phase was confirmed by FFT DPs (Fig. S7e-f). An electron energy loss spectroscopy (Fig. S7g-h) spectrum of the transformed phase shows the loss of peak splitting of Ti $L_{3,2}$ edge, further confirming the TiO phase. A reduction-oxidation (redox) reaction is initiated at the surface of the nanoparticles and advanced from the periphery to the center of the nanoparticles with the orientation relationship of $[010]_A||[010]_{TiO}$, $(002)_A||(020)_{TiO}$ (Fig. S7e and f). This redox process is associated with e-beam sputtering of O atoms [50]. The critical dose rate for this redox process is proposed to be ~4.0 × 10^4 e·nm^{-2}·s^{-1} based on testing of various electron dose rates at room temperature for ~300 s (Fig. 5a-d, Fig. S7-8). Interestingly, this redox reaction depends on crystallographic orientation with respect to the e-beam irradiation direction. The redox reaction is mainly observed in the nanoparticles with $[010]_A$ being parallel with e-beam direction (Fig. 5a-d), while particles with other orientations are relative stable (Fig. 5e-l) with the similar electron dose rate (6 × 10^4 e·nm^{-2}·s^{-1} - 1.1× 10^4 e·nm^{-2}·s^{-1}) and irradiation time (~ 300 s).

We propose this preference of $[010]_A$ for the redox reaction is likely related to the Ti-O bond directions. We calculate the energies needed to displace O atoms along the three e-beam directions using DFT (Fig. 5m-n). The displacement energy E is defined as the energy per length needed to move an atom from its equilibrium position by 0.2 Å

along a specific orientation (please see SI for calculation details). Ti-atom displacements are not considered since they are heavier than O atoms. These calculations can reasonably represent the sputtering of O atoms which are displaced by collision with incoming electrons, whose momentum is along the e-beam direction. Lower energy indicates O-atom displacements are more likely to happen thus facilitating the sputtering.

There are three modes of displacements of O atoms (Fig. 5m), i.e., bending (B), compression (C), and stretching (S) when Ti-O bonds are bent, compressed, and stretched during displacements of O atoms, respectively. In principle, perpendicular alignments between the O atom displacements and the Ti-O bonds define pure B modes, while parallel alignments define pure C or S modes. Here we consider alignments with angles greater than 60° as B modes, and those with angles smaller than 30° as C or S modes, while the rest are mixed modes (Fig. 5n). We find that bending requires the lowest energy when the Ti-O bond has a 90° or near 90° (78°-82°) angle with the e-beam direction. For example, it requires an energy of 0.31 eV/Å to displace an O atom with three B modes (3B) in contrast to 0.91-1.48 eV/Å of combined modes (2B+1C, 2B+1S, or 1B+1C+1S). S mode requires lower energy (0.91eV/Å for modes of 2B+1S, Fig. 5n) than C mode (1.47 eV/Å for modes of 2B+1C, Fig. 5n). Along $[010]_A$: 50% O atoms have all of their three Ti-O bonds perpendicular to the e-beam, and the displacement causes only bond-bending. The other 50% O atoms have one Ti-O bond perpendicular to the e-beam which experiences bending, while the other two are almost parallel with an angle of 12.7° and mainly experience strain (stretching or compression). In comparison, O atoms displaced along $[101]_A$ or $[111]_A$ directions always experience strain in their Ti-O bonds (Fig. 5m), which explains their higher displacement energies.

On average, O atoms need an average of 0.89 eV/Å to be displaced along $[010]_A$, while they need 1.26 and 1.20 eV/Å to be displaced along $[101]_A$ and $[111]_A$ (Fig. 5n), respectively, demonstrating that it is easier to remove O along $[010]_A$ direction, consistent with our experimental observations. Semi in situ TEM enables us to track the structural and morphology evolution of a single particle during a phase transformation process, thus providing missing information about intermediate steps and avoiding the confusion caused by particle aggregation in postmortem experiments. For example, two ABT orientation relationships can be concluded based on the analysis of SEAD patterns of the particles (particle I in Fig. S10, and particle III in Fig. S11) before and after heating experiments; that is, $[001]_A||[001]_B$,$(020)_A||(220)_B$ (Fig. S10) and $[010]_A||[001]_B$,$(002)_A||(110)_B$ (Fig. S11). However, by tracking the particle I, we find that the brookite is very likely transformed from a different particle II, which is in contact with particles I (Fig. S10). Likewise, the brookite in particle III is transformed from particle IV, instead of particle III (Fig. S11). Therefore, the obtained orientation relationship via postmortem experiments may be misleading, while (semi) in situ TEM provides direct evidence of phase transformation relationships and intermediate phases.

In summary, our findings reveal several previously undiscovered pathways of phase transformation among TiO_2 polymorphs (Table 1) under heating or e-beam irradiation. Through in situ observations, we reveal that the growth of new phases can nucleate either at multiple sites in the bulk (e.g., ABT, Fig. S5g), from one side to another side (e.g., anatase to R-phase, Fig. 4), or from the surface to the center of the particles

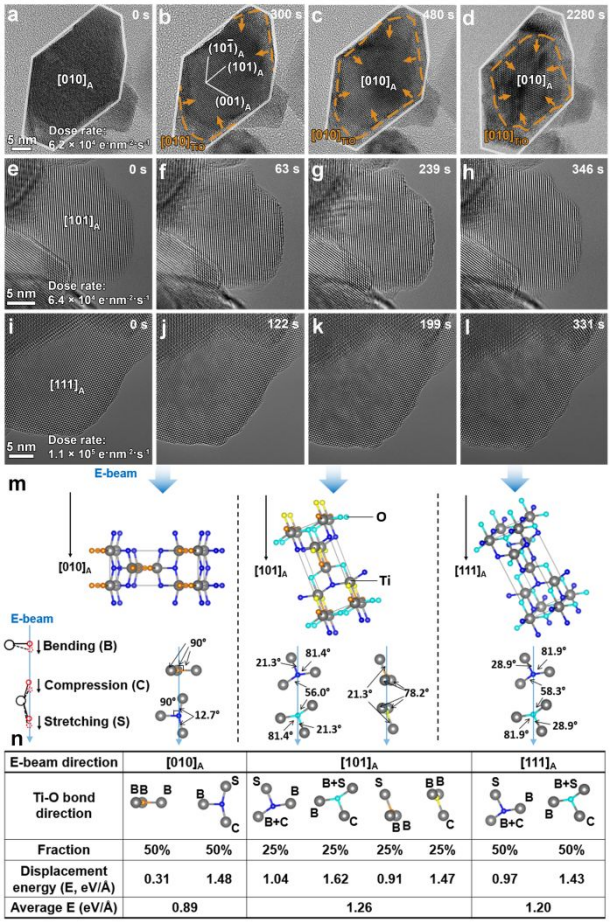

E-beam direction	[010]A		[101]A				[111]A	
Ti-O bond direction	BB B	B S	S B B+C	B+S B C	S B B	B B C	S B B+C	B+S B C
Fraction	50%	50%	25%	25%	25%	25%	50%	50%
Displacement energy (E, eV/Å)	0.31	1.48	1.04	1.62	0.91	1.47	0.97	1.43
Average E (eV/Å)	0.89		1.26				1.20	

Fig. 5 E-beam induced reduction of anatase TiO_2 into TiO at room temperature and its dependence on crystallographic orientation with respect to e-beam irradiation direction. (a–d) Time-sequenced in situ HRTEM images showing the phase transformation from anatase to TiO under irradiation of e-beam with dose rate of 6.2×10^4 e·nm^{-2}·s^{-1}. The edges of the original anatase particle are outlined by white lines. The interface between anatase and TiO are denoted by yellow dashed lines. The phase transformation directions are denoted by yellow arrows. (e–h) and (i–l) Time-sequenced in situ HRTEM images of $[101]_A$ and $[111]_A$ nanoparticles under irradiation of e-beam with dose rate of 6.4×10^4 e·nm^{-2}·s^{-1}and 1.1×10^5 e·nm^{-2}·s^{-1}, respectively. No obvious structure variations were detected. (m) Schematic of e-beam direction with respect to the crystallographic orientation, showing Ti-O bond alignment with e-beam. For each e-beam direction, different colors are used to distinguish O atoms with different displacement modes. (n) Distribution of O atoms with different displacement modes for each direction and their respective displacement energies.

(e.g., anatase to TiO, Fig. 5). Corresponding DFT calculations reveal the feasible atomic structural evolution during the processes. We found that energy barriers of ~0.7-1.0 eV per TiO_2 formula unit need to be overcome in ABT and ART processes, mainly due to (over 16%) Ti-O bond breaking and reformation.

The phase transformation induced by an e-beam is crystallographic orientation dependent with respect to the e-beam irradiation direction in the case that the e-beam is the dominant driving source. For example, at room temperature, small (< 20 nm) anatase nanoparticles can be reduced to TiO. When $[010]_A$ of anatase are aligned with the e-beam direction, it is relatively easier to reduce anatase to TiO because more Ti-O bonds are perpendicular to e-beam direction, making it easier to break Ti-O bonds than $[101]_A$ and $[111]_A$. In addition, with

the e-beam effect, at high temperature (>900°C), anatase can transform into TiO_2 R-phase first and then transform back to anatase but with a crystallographic orientation change.

The obtained understanding of the phase transformation orientation relationships among TiO_2 polymorphs, twining mechanisms, and atomic structural evolution sheds light on interpreting and controlling TiO_2 polymorphs and interface structures for various applications. In situ TEM studies have been used extensively in various fields and provide important information about the kinetics and intermediate steps that cannot be obtained otherwise. However, the electron-beam effect is always a concern during in situ TEM studies. The revealed electron-beam effects revealed in our work provide guidance for in situ TEM studies.

Conflicts of interest

There are no conflicts to declare.

Acknowledgement

The work was conducted in the William R. Wiley Environmental Molecular Sciences Laboratory (EMSL), a national scientific user facility sponsored by the DOE Office of Biological and Environmental Research and located at Pacific Northwest National Laboratory (PNNL). PNNL is a multiprogram national laboratory operated for the U.S. Department of Energy by Battelle under Contract No. DE-AC05-76RLO1830. This research was supported by the U.S. Department of Energy (DOE), Office of Science, Office of Basic Energy Sciences, Early Career Research program under Award KC0203020:67037.

References

1. V. Sencadas, R. Gregorio and S. Lanceros-Méndez, *J Macromol Sci B, Part B*, 2009, **48**, 514-525.
2. F. R. Tay, D. H. Pashley, F. A. Rueggeberg, R. J. Loushine and R. N. Weller, *J. Endod.* 2007, **33**, 1347-1351.
3. J. Diao, K. Gall and M. L. Dunn, *Nat. Mater.*, 2003, **2**, 656-660.
4. D. C. Hurum, A. G. Agrios, K. A. Gray, T. Rajh and M. C. Thurnauer, *J. Phys. Chem. B*, 2003, **107**, 4545-4549.
5. R. Censi and P. Di Martino, *Molecules*, 2015, **20**, 18759-18776.
6. P. Barpanda, T. Ye, M. Avdeev, S.-C. Chung and A. Yamada, *J. Mater. Chem. A*, 2013, **1**, 4194-4197.
7. M. Song, S. Y. He, K. Du, Z. Y. Huang, T. T. Yao, Y. L. Hao, S. J. Li, R. Yang and H. Q. Ye, *Acta Mater*, 2016, **118**, 120-128.
8. T. Luttrell, S. Halpegamage, J. Tao, A. Kramer, E. Sutter and M. Batzill, *Sci. Rep*, 2014, **4**, 4043.
9. A. S. Teja and P.-Y. Koh, *Prog. Cryst. Growth Charact. Mater.* 2009, **55**, 22-45.
10. X. Chen, L. Liu, P. Y. Yu and S. S. Mao, *Science*, 2011, **331**, 746-750.
11. Q. Tay, X. Liu, Y. Tang, Z. Jiang, T. C. Sum and Z. Chen, *J. Phys. Chem. C*, 2013, **117**, 14973-14982.
12. B. Ohtani, O. O. Prieto-Mahaney, D. Li and R. Abe, *J. Photoch. Photobio. A*, 2010, **216**, 179-182.
13. D. Li, F. Soberanis, J. Fu, W. Hou, J. Wu and D. Kisailus, *Cryst. Growth Des*, 2013, **13**, 422-428.
14. R. Wang, K. Hashimoto, A. Fujishima, M. Chikuni, E. Kojima, A. Kitamura, M. Shimohigoshi and T. Watanabe, *Nature*, 1997, **388**, 431-432.
15. M. Setvín, U. Aschauer, P. Scheiber, Y.-F. Li, W. Hou, M. Schmid, A. Selloni and U. Diebold, *Science*, 2013, **341**, 988-991.
16. S. Liu, J. Yu and M. Jaroniec, *Chem. Mater*, 2011, **23**, 4085-4093.
17. E. J. Crossland, N. Noel, V. Sivaram, T. Leijtens, J. A. Alexander-Webber and H. J. Snaith, *Nature*, 2013, **495**, 215-219.
18. X. Wu, Z. Chen, G. Q. M. Lu and L. Wang, *Adv. Funct. Mater*, 2011, **21**, 4167-4172.
19. B. Y. Guan, L. Yu, J. Li and X. W. Lou, *Sci. Adv*, 2016, **2**, e1501554.
20. J. S. Chen, Y. L. Tan, C. M. Li, Y. L. Cheah, D. Luan, S. Madhavi, F. Y. C. Boey, L. A. Archer and X. W. Lou, *J. Am. Chem. Soc.*, 2010, **132**, 6124-6130.
21. F. Rupp, M. Haupt, H. Klostermann, H. S. Kim, M. Eichler, A. Peetsch, L. Scheideler, C. Doering, C. Oehr, H. P. Wendel, S. Sinn, E. Decker, C. von Ohle and J. Geis-Gerstorfer, *Acta Biomater.*, 2010, **6**, 4566-4577.
22. S. Yang, N. Huang, Y. M. Jin, H. Q. Zhang, Y. H. Su and H. G. Yang, *CrystEngComm*, 2015, **17**, 6617-6631.
23. D. H. Kwon, K. M. Kim, J. H. Jang, J. M. Jeon, M. H. Lee, G. H. Kim, X. S. Li, G. S. Park, B.

Lee, S. Han, M. Kim and C. S. Hwang, *Nat. Nanotechnol*, 2010, **5**, 148-153.
24. R. Dong, D. S. Lee, M. B. Pyun, M. Hasan, H. J. Choi, M. S. Jo, D. J. Seong, M. Chang, S. H. Heo, J. M. Lee, H. K. Park and H. Hwang, *Applied Physics A*, 2008, **93**, 409-414.
25. D. A. H. Hanaor and C. C. Sorrell, *J. Mater. Sci.*, 2010, **46**, 855-874.
26. H. Zhang. and B. Jillian F, *J. Mater. Chem.*, 1998, **8**, 2073-2076.
27. A. Gribb Amy and F. Banfield Jillian, *Am. Mineral*, 1997, **82**, 717-728.
28. H. Zhang and J. F. Banfield, *Chem. Mater.*, 2005, **17**, 3421-3425.
29. H. Zhang and F. Banfield Jillian, *J. Phys. Chem. B*, 2000, **104**, 3481-3487.
30. A. S. Barnard and L. A. Curtiss, *Nano Lett.*, 2005, **5**, 1261-1266.
31. W. Dong, Y. Sun, C. W. Lee, W. Hua, X. Lu, Y. Shi, S. Zhang, J. Chen and D. Zhao, *J. Am. Chem. Soc.*, 2007, **129**, 13894-13904.
32. R. L. Penn and F. Banfield Jillian, *Am. Mineral.*, 1999, **84**, 871-876.
33. H. Zhang and F. Banfield Jillian, *J. Am. Ceram. Soc.*, 1999, **84**, 528-535.
34. P. I. Gouma and M. J. Mills, *J. Am. Ceram. Soc.*, 2001, **84**, 619-622.
35. V. Jordan, U. Javornik, J. Plavec, A. Podgornik and A. Rečnik, *Sci. Rep*, 2016, **6**, 24216.
36. V. Jordan, V. D. B. C. Dasireddy, B. Likozar, A. Podgornik and A. Rečnik, *Cryst. Growth Des*, 2018, **18**, 4484-4494.
37. A. Rečnik, N. Stanković and N. Daneu, *Conerib. Mineral. Petr.*, 2015, **169**, 19.
38. N. Daneu, A. Re nik and W. Mader, *Am. Mineral.*, 2014, **99**, 612-624.
39. S. Takeuchi and T. Hashimoto, *J. Mater. Sci*, 1990, **25**, 417-423.
40. H. Wang, Y. Liu, Z. Liu, H. Xu, Y. Deng and H. Shen, *CrystEngComm*, 2012, **14**, 2278-2282.
41. M. Song, G. Zhou, N. Lu, J. Lee, E. Nakouzi, H. Wang and D. Li, *Science*, 2020, **367**, 40-45.
42. H. Zhang and F. Banfield Jillian, *J. Mater. Chem*, 1998, **8**, 2073-2076.
43. W. Y. Lee, P. D. Bristowe, Y. Gao and K. L. Merkle, *Philos. Mag*, 1993, **68**, 309-314.
44. P. I. Gouma and M. J. Mills, *J. Am. Ceram. Soc.*, 2001, **84**, 619-622.
45. J. W. Christian and S. Mahajan, *Prog. Mater. Sci.*, 1995, **39**, 1-157.
46. Y. T. Zhu, X. Z. Liao and X. L. Wu, *JOM*, 2008, **60**, 60-64.
47. R. L. Penn and J. F. Banfield, *Am. Mineral.*,1998, **83**, 1077-1082.
48. A. Lotnyk, S. Senz and D. Hesse, *Thin Solid Films*, 2007, **515**, 3439-3447.
49. M. Song and D. Li, *Microsc. Microanal.* 2019, **25**, 1868-1869.
50. R. F. Egerton, P. Li and M. Malac, *Micron* 2004, ***35***, 399-409.

TOC:

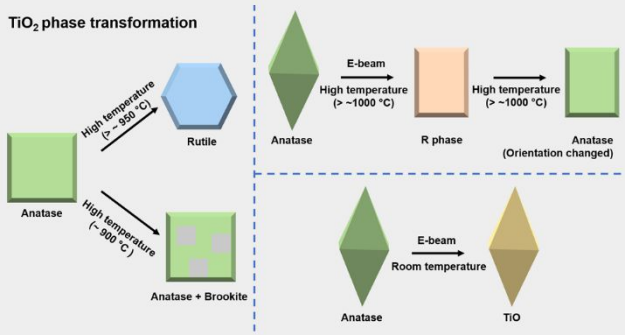
TiO2 phase transformation
High temperature
(> ~ 950 °C)
Rutile
Anatase
High temperature
(~ 500 °C)
Anatase + Brookite
E-beam
High temperature
(> ~1000 °C)
Anatase
R phase
High temperature
(> ~1000 °C)
Anatase
(Orientation changed)
E-beam
Room temperature
Anatase
TiO